Keck HIRES spectroscopy of SkyMapper commissioning survey candidate extremely metal-poor stars

A. F. Marino [1,2,3]★ G. S. Da Costa [1] A. R. Casey [1,4,5] M. Asplund [1,6]
M. S. Bessell [1] A. Frebel [7] S. C. Keller,[1] K. Lind,[8,9] A. D. Mackey,[1]
S. J. Murphy [1,10] T. Nordlander,[1,6] J. E. Norris,[1] B. P. Schmidt [1] and D. Yong [1]

[1]*Research School of Astronomy & Astrophysics, Australian National University, ACT 2611, Australia*
[2]*Dipartimento di Fisica e Astronomia 'Galileo Galilei' – Univ. di Padova, Vicolo dell'Osservatorio 3, Padova, IT-35122, Italy*
[3]*Centro di Ateneo di Studi e Attività Spaziali 'Giuseppe Colombo' – CISAS, Via Venezia 15, Padova, IT-35131, Italy*
[4]*School of Physics and Astronomy, Monash University, Wellington Rd, Clayton, VIC 3800, Australia*
[5]*Faculty of Information Technology, Monash University, Wellington Rd, Clayton, VIC 3800, Australia*
[6]*Center of Excellence for Astrophysics in Three Dimensions (ASTRO-3D), Australia*
[7]*Department of Physics and Kavli Institute for Astrophysics and Space Research, Massachusetts Institute of Technology, Cambridge, MA 02139, USA*
[8]*Max-Planck-Institut für Astronomie, Königstuhl 17, D-69117 Heidelberg, Germany*
[9]*Observational Astrophysics, Department of Physics and Astronomy, Uppsala University, Box 516, SE-751 20 Uppsala, Sweden*
[10]*School of Physical, Environmental and Mathematical Sciences, University of New South Wales, Canberra, ACT 2600, Australia*

ABSTRACT

We present results from the analysis of high-resolution spectra obtained with the Keck HIRES spectrograph for a sample of 17 candidate extremely metal-poor (EMP) stars originally selected from commissioning data obtained with the SkyMapper telescope. Fourteen of the stars have not been observed previously at high dispersion. Three have [Fe/H] ≤ -3.0, while the remainder, with two more metal-rich exceptions, have $-3.0 \leq$ [Fe/H] ≤ -2.0 dex. Apart from Fe, we also derive abundances for the elements C, N, Na, Mg, Al, Si, Ca, Sc, Ti, Cr, Mn, Co, Ni, and Zn, and for n-capture elements Sr, Ba, and Eu. None of the current sample of stars is found to be carbon-rich. In general, our chemical abundances follow previous trends found in the literature, although we note that two of the most metal-poor stars show very low [Ba/Fe] (~ -1.7) coupled with low [Sr/Ba] (~ -0.3). Such stars are relatively rare in the Galactic halo. One further star, and possibly two others, meet the criteria for classification as a r-I star. This study, together with that of Jacobson et al. (2015), completes the outcomes of the SkyMapper commissioning data survey for EMP stars.

Key words: stars: abundances – stars: Population II – Galaxy: halo – Galaxy: stellar content.

1 INTRODUCTION

As reviewed by Frebel & Norris (2015), the detailed study of the most metal-poor stars in the Galaxy can provide vital clues to the processes of star formation and to the synthesis of the chemical elements at the earliest times. Such stars, however, are extremely rare and at the present time only a handful are known with [Fe/H] ≤ -4.5 dex. The importance of these objects has nevertheless prompted a number of previous and ongoing searches for such extremely metal-poor (EMP) stars [e.g. the HK survey (Beers, Preston & Shectman 1992), the HES (Frebel et al. 2006; Christlieb et al. 2008), the SDSS (see Aoki et al. 2013), the 'Best and Brightest' survey (Schlaufman & Casey 2014), LAMOST (see Li et al. 2015a),

and Pristine (Starkenburg et al. 2017), and references therein]. The discovery of such stars is one of the prime science drivers behind the SkyMapper imaging survey of the Southern hemisphere sky (Keller et al. 2007; Wolf et al. 2018). The metallicity sensitivity is achieved through the incorporation of a relatively narrow v-filter, whose bandpass includes the Ca II H and K lines, into the SkyMapper filter set (Bessell et al. 2011). The SkyMapper $uvgriz$ photometric survey of the southern sky is ongoing (Wolf et al. 2018) but during the commissioning of the telescope a number of vgi images were taken to search for EMP candidates. Despite the sub-optimal quality of many of the images, the program, which we will refer to as the 'SkyMapper commissioning survey for EMP-stars' (to distinguish it from the current ongoing work), was successful in that it resulted in the discovery of the currently most-iron poor star known SMSS J031300.36–670839.3 (Keller et al. 2014; Bessell et al. 2015; Nordlander et al. 2017). The analysis

★ E-mail: anna.marino@unipd.it

Table 1. Details of the target stars and the Keck HIRES observations.

ID	RA (J2000)(^{h}:^{m}:^{s})	Dec. (J2000)($^\circ$:$'$:$''$)	g	$(g-i)_0$	m_i	Exp Time (s)	S/N [450 nm] (pix^{-1})	S/N [600 nm] (pix^{-1})	RV (km s^{-1})	Notes
SMSS J202059.17–043447.0	20:20:59.17	− 04:34:47.0	13.815	0.837	0.243	660	34	38	− 190.7	
SMSS J202400.03–024445.9	20:24:00.03	− 02:44:45.9	15.631	0.850	0.235	660	15	17	− 133.8	
SMSS J202601.44–033002.5	20:26:01.44	− 03:30:02.5	15.508	0.541	0.140	1800	21	26	− 149.5	
SMSS J202659.41–031149.2	20:26:59.41	− 03:11:49.2	14.180	0.641	0.027	600	28	29	− 199.1	
SMSS J204654.92–020409.2	20:46:54.92	− 02:04:09.2	15.026	0.882	0.131	1200	26	30	− 451.2	
SMSS J211657.83–012517.5	21:16:57.83	− 01:25:17.5	14.515	0.675	− 0.054	900	21	22	− 155.4	
SMSS J212001.71–001158.6	21:20:01.71	− 00:11:58.6	15.582	0.942	0.134	1500	22	26	− 350.2	
SMSS J212113.63–005132.2	21:21:13.63	− 00:51:32.2	14.854	0.712	0.002	1200	21	23	+33.9	
SMSS J212217.52–295552.7	21:22:17.52	− 29:55:52.7	16.387	0.554	0.040	2700	18	19	+200.8	
SMSS J220514.10–013407.6	22:05:14.10	− 01:34:07.6	13.933	0.802	0.225	600	22	26	− 199.2	
SMSS J220535.05–004403.6	22:05:35.05	− 00:44:03.6	14.214	0.704	0.043	600	25	28	− 62.2	
SMSS J221334.13–072604.1	22:13:34.13	− 07:26:04.1	15.310	0.759	0.072	1500	19	22	− 392.7	1
SMSS J222349.48–114751.1	22:23:49.48	− 11:47:51.1	15.177	0.719	0.028	1500	22	23	− 367.1	
SMSS J225336.83–270435.4	22:53:36.83	− 27:04:35.4	16.024	0.685	0.022	1500	16	17	+116.6	
SMSS J230306.22–041621.8	23:03:06.22	− 04:16:21.8	14.606	0.699	0.003	1200	26	28	− 244.6	
SMSS J010839.58–285701.5	01:08:39.58	− 28:57:01.5	12.747	0.615	0.033	300	34	35	+144.3	2
SMSS J034249.52–284215.8	03:42:49.52	− 28:42:15.8	14.646	0.676	0.108	1200	29	31	+157.2	2

Notes: (1) In Aoki et al. (2013) as SDSS J2213–0726; and (2) in Jacobson et al. (2015)
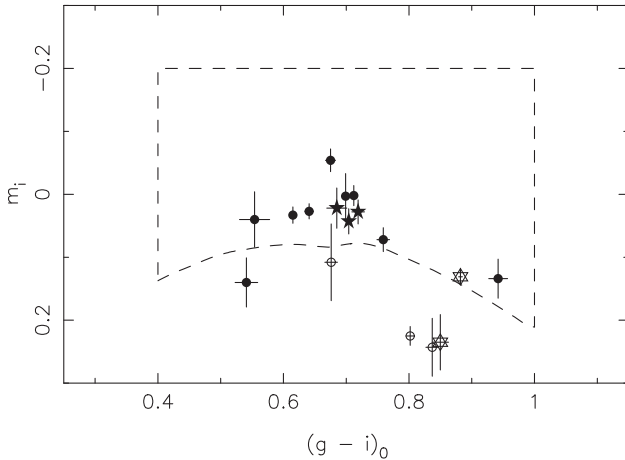
Figure 1. The location of the stars observed with Keck in the SkyMapper metallicity sensitive diagram using DR1.1 photometry. The selection window currently employed to select candidate EMP stars is shown by the dashed boundary. Stars whose abundances are determined here to have [Fe/H]$_{\rm LTE}$ ≤ −3.0 are plotted as filled star symbols, those with −3.0 ≤ [Fe/H]$_{\rm LTE}$ ≤ −2.5 are plotted as filled circles, open circles show stars with −2.5 ≤ [Fe/H]$_{\rm LTE}$ ≤ −2.0, and the 6-point star symbol shows the star for which [Fe/H]$_{\rm LTE}$ > −2.0 dex. Individual error bars are shown. These have been calculated from the photometry errors given in the DR1.1 database.

of high dispersion spectra of a large sample of additional EMP-candidates selected from the commissioning survey was presented in Jacobson et al. (2015). Here we present the final results from that survey – the outcome of high dispersion spectroscopic observations of a further sample of SkyMapper EMP-candidates drawn from the commissioning survey photometry. SkyMapper commissioning-era photometry was also employed in the search for EMP stars in the Galactic Bulge (Howes et al. 2015, 2016).

The paper is organized as follows. The following section describes the target selection, the observations, and the data-reduction process. Section 3 then describes the determination of the atmospheric parameters for the stars and the subsequent analysis to derive the chemical abundances. The abundance results

are compared with existing halo EMP-star studies, such as those of Yong et al. (2013), Placco et al. (2014), and Jacobson et al. (2015), in Section 4. The results are briefly summarized in Section 5.

2 TARGET SAMPLE AND OBSERVATIONS

As discussed briefly in Jacobson et al. (2015), the initial sample of EMP candidates was selected on the basis of location in a two-colour diagram in which a photometric metallicity index $m_i = (v - g)_0 - 1.5(g - i)_0$ is plotted against $(g - i)_0$ (see also Keller et al. 2007). Because of the variable quality of the commissioning-epoch data, and because of the calibration approach employed, the photometric candidate list required additional input to identify the best candidates for high dispersion spectroscopic follow-up. This was achieved by obtaining low-resolution ($R \approx 3000$) spectra of the candidates with the WiFeS spectrograph (Dopita et al. 2010) on the ANU 2.3 m telescope at Siding Spring Observatory. The resulting flux calibrated spectra, which cover the wavelength range ∼350–600 nm, are then compared with a grid of MARCS 1D model atmosphere fluxes and the best-fitting determined, as described in Norris et al. (2013). Because the spectra cover the Paschen continuum as well as the Balmer jump and the Balmer lines of hydrogen, the best-fitting temperature and gravity are generally well determined. Consistency with the temperature/gravity relation for an old metal-poor isochrone,[1] which is appropriate for halo stars, provides a constraint on the adopted reddening while the strengths of metal-lines such as Ca II H and K and Mg I b provide the metallicity information for a given temperature and gravity. The outcome of the 2.3 m spectroscopy is then a sample of EMP candidates that can be used with some confidence as a basis for follow-up studies at high dispersion.

The candidates observed with the HIRES spectrograph (Vogt et al. 1994) at the Keck-I telescope were those in the commissioning survey EMP candidate sample that had not been previously observed at high dispersion (cf. Jacobson et al. 2015), which

---

[1] The isochrones employed are those from VandenBerg, Bergbusch & Dowler (2006) supplemented with additional isochrones for metallicities below [Fe/H] = −2.3 dex (Vandenberg, private communication 2009).
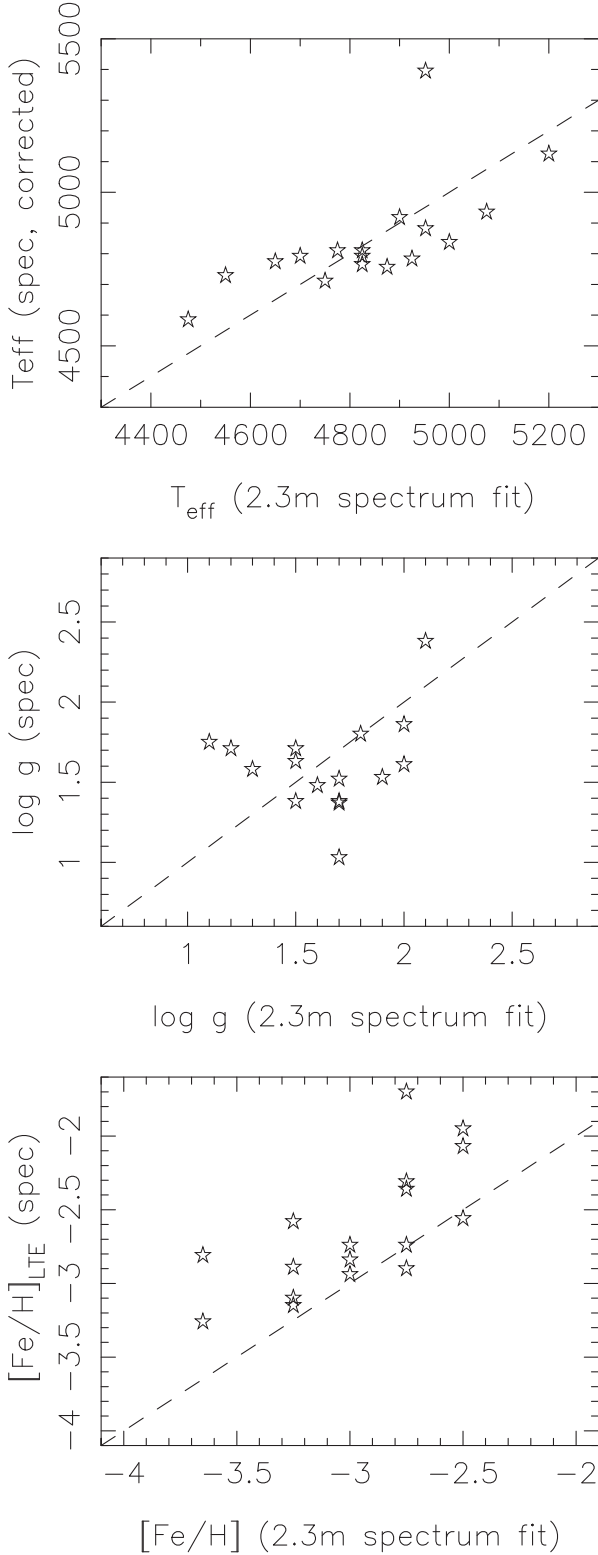
Figure 2. *Top panel*: the adopted corrected spectroscopic temperatures are shown as a function of the temperatures obtained from spectral fits to the low-resolution 2.3 m spectra. The dashed line is the 1:1 relation. *Middle panel*: the adopted spectroscopic gravities are plotted against the log *g* values derived from the fits to the low-resolution spectra. The dashed line is the 1:1 relation. *Bottom panel*: a comparison of the $[\text{Fe/H}]_{\text{LTE}}$ values determined from the Keck spectra with those estimated from the low-resolution spectral fits. The dashed line is again a 1:1 relation.

were accessible from the Keck Observatory on the scheduled date and which had low-resolution spectroscopic abundance estimates $[\text{Fe/H}]_{2.3m} \leq -2.5$ dex, as determined from the 2.3m spectra. In all, HIRES spectra were obtained for 15 candidate EMP stars on the ANU-allocated night of 2013 September 21 (UT), together with spectra of two stars that had also been observed at Magellan with the MIKE spectrograph in the Jacobson et al. (2015) study. One further star, SMSS J221334.13–072604.1, was subsequently found to be included in the sample analysed by Aoki et al. (2013) under the designation SDSS J2213–0726.

Observing conditions were good with the seeing slowly rising from 0.6 to 1 arcsec by the end of the night. The spectrograph was configured with the HIRESb cross-disperser and the C1 decker that has a slit width of 0.86 arcsec yielding a resolution $R \approx 50\,000$. Detector binning was 2 (spatial) × 1 (spectral) and the low-gain setting ($\sim 2e^-/$DN) was used for the three CCDs in the detector mosaic. Details of the observations are given in Table 1. The table lists the SkyMapper survey designations, the positions, and the SkyMapper g, $(g - i)_0$ and m_i photometry taken from the SkyMapper DR1.1 data release (Wolf et al. 2018), which supersede the original commissioning-era photometry. The reddening corrections follow the procedure outlined in Wolf et al. (2018) while m_i is the metallicity index, defined as $(v - g)_0 - 1.5(g - i)_0$, for which more negative values at fixed colour indicate potentially lower metallicity (see Keller et al. 2007; Da Costa et al.). Also given are the integration times and the S/N per pixel of the reduced spectra at 450 and 600 nm. The median values are 22 pix^{-1} at 450 nm and 26 pix^{-1} at 600 nm.

In Fig. 1 we show the location of the observed stars in the SkyMapper metallicity-sensitive diagram based on the DR1.1 photometry. Shown also in the figure is the selection window that is used in defining photometric EMP candidates for the current (post-commissioning) survey, where the lower boundary is set by the location of the [M/H] $= -2.0$ dex, 12.5 Gyr isochrone in this plane (see Da Costa et al., in preparation for details). While photometric uncertainties, particularly in the v-magnitudes, introduce scatter in this diagram, it is reassuring that all but 1 of the 12 candidates that are found in the analysis here to have $[\text{Fe/H}]_{\text{LTE}} \leq -2.5$ dex (where LTE means that the Fe abundance is obtained assuming the local thermodynamic equilibrium, LTE) are within the selection window while there is only one contaminant – a star found here to have $[\text{Fe/H}]_{\text{LTE}} > -2.0$ despite lying (just) in the selection region. Although the sample is small, Fig. 1 does verify that the current SkyMapper photometric selection process efficiently finds stars with $[\text{Fe/H}]_{\text{LTE}} \leq -2.5$ with only a very minor degree of contamination. In fact, Da Costa et al. () show that in the current ongoing program, $\sim$85 per cent of the SkyMapper DR1.1 photometric EMP candidates that lie within the selection window shown in Fig. 1, and which also possess metallicity estimates from low-resolution 2.3 m spectra, have $[\text{Fe/H}]_{2.3m} \leq -2.0$ dex, while $\sim$40 per cent have $[\text{Fe/H}]_{2.3m} \leq -2.75$ dex. The best candidates are then followed up at high dispersion with the MIKE echelle spectrograph on the Magellan 6.5 m telescope.

The observed spectra were processed with the standard HIRES reduction pipeline MAKEE to obtain flat-fielded, extracted, wavelength-calibrated, velocity-corrected spectra for each echelle order. For the subsequent analysis, the individual spectral orders were merged into a single continuous spectrum for each of the three CCD detectors, which was then continuum normalized and wavelength-offset by the observed geocentric velocity.

Radial velocities (RVs) were derived using the IRAF@FXCOR task, which cross-correlates the object spectrum with a template

Table 2. Adopted atmospheric parameters $T_{\rm eff}$/log g/[Fe/H]$_{\rm LTE}$/$\xi_{\rm t}$. [Fe/H]$_{\rm non\text{-}LTE}$ obtained values are also listed.

ID	$T_{\rm eff}$ K	log g dex	[Fe/H]$_{\rm LTE}$ dex	[Fe/H]$_{\rm non\text{-}LTE}$ dex	$\xi_{\rm t}$ km s^{-1}
SMSS J202059.17–043447.0	4711	1.38	−2.30	−2.17	1.64
SMSS J202400.03–024445.9	4792	1.71	−1.97	−1.88	1.98
SMSS J202601.44–033002.5	5125	2.38	−2.84	−2.72	1.55
SMSS J202659.41–031149.2	4918	1.80	−2.94	−2.78	1.74
SMSS J204654.92–020409.2	4729	1.75	−1.71	−1.62	1.70
SMSS J211657.83–012517.5	4837	1.61	−2.56	−2.42	1.95
SMSS J212001.71–001158.6	4585	1.03	−2.58	−2.43	2.45
SMSS J212113.63–005132.2	4810	1.53	−2.75	−2.58	1.95
SMSS J212217.52–295552.7	5395	3.17	−2.81	−2.73	2.15
SMSS J220514.10–013407.6	4774	1.63	−2.07	−1.97	1.80
SMSS J220535.05–004403.6	4765	1.38	−3.10	−2.91	1.85
SMSS J221334.13–072604.1	4810	1.52	−2.89	−2.72	1.97
SMSS J222349.48–114751.1	4756	1.37	−3.15	−2.96	1.86
SMSS J225336.83–270435.4	4882	1.71	−3.26	−3.07	2.32
SMSS J230306.22–041621.8	4792	1.48	−2.74	−2.58	1.72
SMSS J010839.58–285701.5	4936	1.86	−2.90	−2.76	1.68
SMSS J034249.52–284215.8	4783	1.58	−2.31	−2.19	1.70

Table 3. Atomic data and EWs for program stars.

Wavelength [Å]	Species	E.P. [eV]	log(gf)	EW [mÅ]
		SMSS J202059.17–043447.0		
4447.720	26.0	2.220	−1.340	80.0
4595.360	26.0	3.290	−1.760	19.2
4602.940	26.0	1.490	−2.210	90.0
4630.120	26.0	2.280	−2.590	20.9
4733.590	26.0	1.490	−2.990	55.0
4736.770	26.0	3.210	−0.750	60.9
4871.320	26.0	2.870	−0.360	91.7
4903.310	26.0	2.880	−0.930	69.4
4918.990	26.0	2.850	−0.340	91.1
4924.770	26.0	2.280	−2.110	51.4
4938.810	26.0	2.880	−1.080	56.7
4939.690	26.0	0.860	−3.250	77.7
4966.090	26.0	3.330	−0.870	45.0
4994.130	26.0	0.920	−2.970	88.6
5014.940	26.0	3.940	−0.300	37.7
5044.210	26.0	2.850	−2.020	13.8

Notes: Only a portion of this table is shown here to demonstrate its form
and content. A machine-readable version of the full table will be online
available.

spectrum. For the template, we used a synthetic spectrum obtained
through the 2014 June version of MOOG (Sneden 1973). This
spectrum was computed with a stellar model atmosphere interpo-
lated from the Castelli & Kurucz (2004) grid, adopting parameters
(effective temperature $T_{\rm eff}$, surface gravity log g, microturbulence
$\xi_{\rm t}$, metallicity [M/H]) = (4800 K, 1.5, 2.0 km s^{-1}, −2.50). The
errors associated with RVs due to the cross-correlation technique are
generally small, and in our case are between ∼0.2 and ∼0.6 km s^{-1}.
As we do not have repeated observations of the same star, we
cannot provide more realistic estimates of the internal velocity
uncertainties.

Independent radial velocity measurements are available for four
of our stars: the two in common with Jacobson et al. (2015)
(SMSS J010839.58–285701.5 and SMSS J034249.52–284215.8),
the star in common with Aoki et al. (2013), and the star
SMSS J202059.17–043447.0, which has a radial velocity tabulated
in Gaia DR2 (Gaia Collaboration 2018). SMSS J010839.58–

285701.5 also has a radial velocity listed in Gaia DR2. Comparison
with these independent values reveals that a correction of −84 ± 2
(standard error of the mean) km s^{-1} to our velocities is required
for agreement. We can find no obvious explanation for this velocity
offset but have verified its existence via an independent reduction
of a subset of the observed spectra. With the offset applied, our
velocities agree well with the published values, and there is no
evidence for any significant velocity variability in these four stars.
Table 1 then lists the heliocentric radial velocity for each star in our
sample after applying the velocity offset. Many of the stars have
large heliocentric velocities as expected for a sample dominated by
Galactic halo stars.

3 CHEMICAL ABUNDANCES ANALYSIS

Chemical abundances were derived from an LTE analysis by using
the 2014 June version of the spectral analysis code MOOG (Sneden
1973), together with the alpha-enhanced Kurucz model atmospheres
of Castelli & Kurucz (2004), whose parameters have been obtained
as described in Section 3.1. The reference solar abundances adopted
were those of Asplund et al. (2009).

In the following sections we detail the approach employed
to derive the adopted atmospheric parameters, and describe the
spectral features used to infer the chemical abundances. In general,
we follow the procedures outlined in Jacobson et al. (2015) in order
to facilitate a direct comparison of the results obtained here with
those in that work.

3.1 Atmospheric parameters

The atmospheric parameters were derived via a number of different
steps. First, as in Jacobson et al. (2015), initial values of $T_{\rm eff}$ and
the microturbulence $\xi_{\rm t}$ were determined by imposing excitation
potential (E.P.) equilibrium for Fe I, to yield $T_{\rm eff}$, and by removing
any trend between Fe I abundance and the reduced equivalent width
(EW) to fix $\xi_{\rm t}$. For the majority of the stars observed, however, there
was a paucity of measureable Fe II lines in the spectra invalidating
the determination of a spectroscopic log g value by matching Fe I
and Fe II abundances. Instead, we derived log g by matching the $T_{\rm eff}$
value with a 12 Gyr Yonsei–Yale isochrone (Demarque et al. 2004)
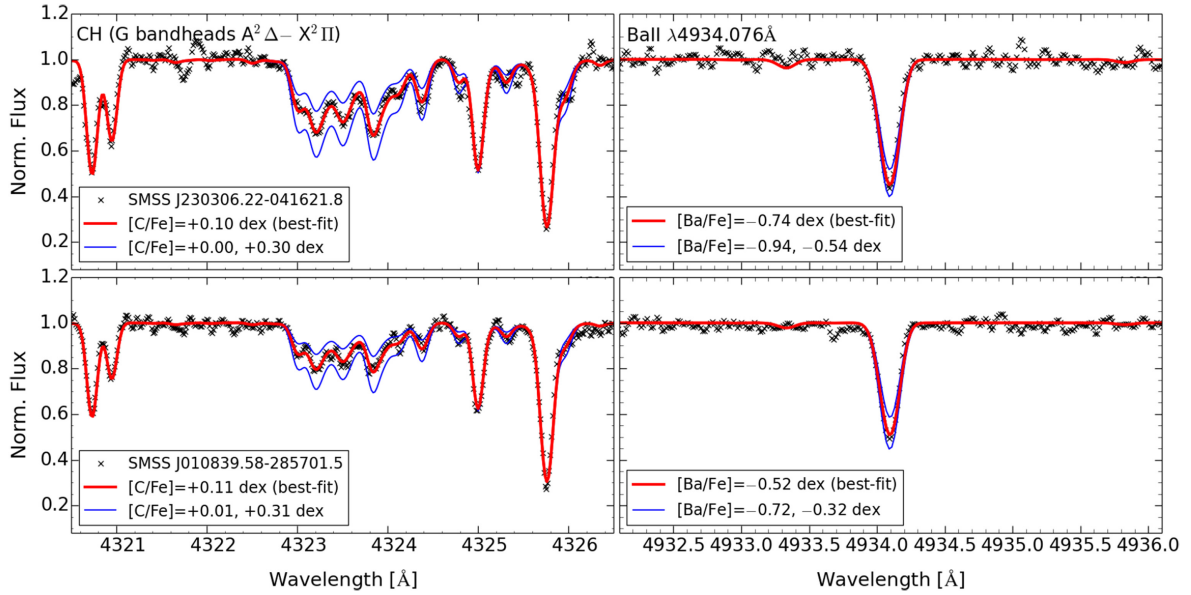
Figure 3. *Left-hand panels:* synthetic spectra fits to the CH features in the vicinity of 4323 Å, one of two spectral regions used to determine the carbon abundance. For each star the observations are shown as black crosses, the best-fit is shown by the thick red line while the thin blue lines show [C/Fe] values 0.2 dex larger and 0.1 dex smaller than the best-fitting value. *Right-hand panels:* synthetic spectra fits to the Ba II line at 4934.1 Å, one of two (or three) lines used to determine the barium abundance. Again the observations are shown as black crosses, the best-fit is the red thick line, and the thin blue lines show [Ba/Fe] values ±0.2 dex about the best-fitting value.

Table 4. Chemical abundance ratios for the light elements C, N, Na, and Al. For carbon we also list the evolutionary corrected [C/Fe]$_{evol}$ abundances derived by applying corrections from V. Placco (private communication); the estimated natal [C/Fe] corresponds to [C/Fe]$_{evol}$. For sodium we give both LTE and non-LTE abundances. We also report the number (#) of spectral features analysed for each element as well as the standard deviations of the abundances (σ).

ID	[C/Fe]	σ	#	[C/Fe]$_{evol}$	[N/Fe]	σ	#	[Na/Fe]$_{LTE}$	σ	[Na/Fe]$_{non\text{-}LTE}$	σ	#	[Al/Fe]	σ	#
SMSS J202059.17–043447.0	−0.20	0.01	2	0.39	0.92	0.24	2	0.16	0.18	−0.10	0.04	3	−0.44	–	1
SMSS J202400.03–024445.9	−0.40	0.03	2	−0.09	0.94	0.16	2	0.21	0.08	−0.18	0.06	2	−1.00	–	1
SMSS J202601.44–033002.5	0.18	0.02	2	0.19	–	–	–	0.27	0.09	−0.09	0.03	2	−0.68	0.11	2
SMSS J202659.41–031149.2	−0.06	0.03	2	0.07	–	–	–	0.44	0.03	0.04	0.01	2	−0.54	0.23	2
SMSS J204654.92–020409.2	−0.42	0.01	2	−0.15	0.53	0.08	2	−0.28	0.10	−0.46	0.04	4	–	–	–
SMSS J211657.83–012517.5	0.05	0.02	2	0.43	–	–	–	0.23	0.10	−0.16	0.10	2	−0.83	0.15	2
SMSS J212001.71–001158.6	−0.49	0.02	2	0.25	1.13	0.34	2	0.12	0.04	−0.17	0.04	2	–	–	–
SMSS J212113.63–005132.2	0.26	0.03	2	0.66	–	–	–	0.45	0.03	0.05	0.01	2	−0.40	0.35	2
SMSS J212217.52–295552.7	0.64	0.05	2	0.64	–	–	–	0.38	0.08	0.00	0.09	2	–	–	–
SMSS J220514.10–013407.6	−0.09	0.03	2	0.27	0.80	0.16	2	0.07	0.18	−0.21	0.08	3	−0.96	–	1
SMSS J220535.05–004403.6	−0.01	0.01	2	0.51	–	–	–	0.24	0.17	−0.02	0.09	2	−0.67	0.18	2
SMSS J221334.13–072604.1	−0.58	0.01	2	−0.15	–	–	–	0.04	0.05	−0.22	0.01	2	−0.60	–	1
SMSS J222349.48–114751.1	−0.22	0.01	2	0.31	–	–	–	0.73	0.13	0.36	0.08	2	−0.65	0.14	2
SMSS J225336.83–270435.4	0.20	0.03	2	0.37	–	–	–	0.13	0.08	−0.07	0.02	2	−0.63	–	1
SMSS J230306.22–041621.8	0.12	0.02	2	0.56	–	–	–	0.22	0.04	−0.12	0.08	2	−0.10	–	1
SMSS J010839.58–285701.5	0.12	0.01	2	0.22	–	–	–	0.71	0.11	0.23	0.06	2	−0.22	0.09	2
SMSS J034249.52–284215.8	−0.41	0.01	2	0.03	–	–	–	−0.44	0.07	−0.71	0.03	2	−1.34	0.49	2

that has [α/Fe] = +0.4 and the appropriate metallicity for the star as derived from the initial analysis. The procedure was then iterated until the T_{eff}, log g, and ξ_t values did not change appreciably – usually only one iteration was required.

However, as noted by Jacobson et al. (2015, and the references therein), spectroscopic T_{eff} values for metal-poor red giants are generally cooler than those inferred from photometry due to departures from LTE. Jacobson et al. (2015) dealt with this issue by adopting corrections to the spectroscopic effective temperatures as described in Frebel et al. (2013). These corrections shift the spectroscopic temperatures to a scale that is more consistent with photometrically derived temperatures. Such a shift is also supported

by the recent detailed 3D non-LTE calculations for Fe (Amarsi et al. 2016) and H (Amarsi et al. 2018). Consequently, in order to allow direct comparison of the abundances derived here with those of Jacobson et al. (2015), we have followed the same approach: the spectroscopic T_{eff} values have been corrected as described in Frebel et al. (2013), leading to updated values of ξ_t and the isochrone-based log g values. Again the process was iterated until convergence was achieved, and the resulting values used in the abundance analysis. In the end, the corrections applied to the spectroscopic T_{eff} ranged between ∼150 and ∼220 K, being larger for the cooler stars.

We can verify the suitability of the final adopted stellar parameters by comparing them with the T_{eff} and log g values derived from

Table 5. Chemical abundances for α elements, Mg, Si, Ca, and Ti. For each element we report the number (#) of analysed spectral features and the resulting standard deviations (σ).

ID	[Mg/Fe]	σ	#	[Si/Fe]	σ	#	[Ca/Fe]	σ	#	[Ti I/Fe]	σ	#	[Ti II/Fe]	σ	#
SMSS J202059.17–043447.0	0.40	0.05	3	0.43	0.18	2	0.35	0.19	2	0.10	0.07	6	0.37	0.10	8
SMSS J202400.03–024445.9	0.63	0.23	3	0.42	0.01	2	0.58	0.30	2	0.19	0.09	5	0.38	0.13	8
SMSS J202601.44–033002.5	0.42	0.01	2	0.57	0.19	2	0.46	–	1	0.45	0.19	2	0.10	0.13	5
SMSS J202659.41–031149.2	0.42	0.12	2	0.75	0.32	2	0.39	0.01	2	0.39	0.16	2	0.43	0.17	7
SMSS J204654.92–020409.2	0.19	0.16	3	0.18	0.15	2	0.34	0.16	3	−0.01	0.06	7	0.25	0.12	8
SMSS J211657.83–012517.5	0.47	0.07	2	0.56	0.43	2	0.34	0.02	2	0.30	0.15	4	0.03	0.18	8
SMSS J212001.71–001158.6	0.36	0.12	2	0.69	0.15	2	0.36	0.07	2	0.20	0.08	5	0.25	0.15	8
SMSS J212113.63–005132.2	0.35	0.04	2	0.64	0.46	2	0.33	0.21	2	0.38	0.01	2	0.00	0.15	7
SMSS J212217.52–295552.7	0.21	0.09	2	0.87	–	1	–	–	–	–	–	–	−0.21	0.04	2
SMSS J220514.10–013407.6	0.43	0.16	3	0.28	0.33	2	0.37	0.03	2	0.22	0.04	6	0.31	0.13	8
SMSS J220535.05–004403.6	0.26	0.19	2	0.72	0.36	2	0.21	–	1	0.28	0.17	2	0.21	0.09	3
SMSS J221334.13–072604.1	0.31	0.18	2	0.70	0.03	2	0.38	0.03	2	0.46	0.33	2	0.26	0.17	6
SMSS J222349.48–114751.1	0.47	0.00	2	0.60	0.18	2	0.45	–	1	0.43	0.15	2	0.35[(1)]	0.20	5
SMSS J225336.83–270435.4	0.32	0.25	2	0.58	0.14	2	0.48	–	1	–	–	–	0.03[(1)]	0.03	2
SMSS J230306.22–041621.8	0.48	0.01	2	0.75	0.25	2	0.45	0.03	2	0.32	0.10	5	0.15	0.10	7
SMSS J010839.58–285701.5	0.40	0.15	3	0.74	0.27	2	0.43	–	1	0.37	0.11	7	0.34	0.08	6
SMSS J034249.52–284215.8	−0.24	0.06	2	0.11	0.29	2	−0.08	0.01	2	−0.28	0.08	4	−0.20	0.09	8

Notes: (1) Given the lack of Fe II abundances, Fe I has been used for the Ti II abundances relative to Fe.

the spectrophotometric fits to the 2.3 m low-resolution spectra. The comparison is shown in the upper panels of Fig. 2. The top panel compares the corrected spectroscopic $T_{\rm eff}$ values with the spectrophotometric determinations: it shows excellent agreement – the points scatter about the 1:1 line and the mean difference between the determinations is only 10 K (spectroscopic $T_{\rm eff}$ hotter) with a standard deviation of 150 K. Ascribing equal uncertainties to each method then indicates that the uncertainty in the adopted spectroscopic $T_{\rm eff}$ values is of order 100 K. The largest discrepancy occurs for star SMSS J212217.52–295552.7 where the corrected spectroscopic temperature is ∼450 K hotter than the spectrophotometric determination. There is no straightforward explanation for this difference although we note that, based on the other stars in the sample, the spectrophotometric temperature for this star is too cool by ∼200 K for its $(g − i)_0$ colour. We also note that with $g \approx 16.4$, this star is fainter than the usual $g = 16$ limit for 2.3m follow-up observations, while the HIRES observations have one of the lowest S/N values in the sample. For consistency of approach we retain the use of the corrected spectroscopic temperature for this star, although the uncertainty is likely larger than the typical ±100 K value.

The middle panel shows the comparison for the log g values. Here the mean difference, in the sense $\log g_{2.3m} − \log g_{\rm spec}$, is +0.05 dex with a standard deviation of 0.35 dex after excluding SMSS J212217.52–295552.7 where the large difference in temperature and our isochrone-based approach to fix $\log g_{\rm spec}$, results in a significant offset from the spectrophotometric value. Again assuming equal uncertainties in each method, this suggests that the uncertainty in the adopted log g values is of order of ∼0.25 dex. The adopted atmospheric parameters and the resulting [Fe/H]$_{\rm LTE}$ values are given in Table 2. Together with the [Fe/H]$_{\rm LTE}$, we list the [Fe/H]$_{\rm non-LTE}$ values obtained by applying non-LTE corrections to Fe I lines as in Lind, Bergemann & Asplund (2012) and Lind et al. (2017). For comparison reasons, in the following we will use our [Fe/H]$_{\rm LTE}$ values.

An independent check on the adopted atmospheric parameters is provided by a comparison with those adopted in Jacobson et al. (2015) for the two stars in common. For SMSS J010839.58–285701.5 we find $T_{\rm eff}$/log g/[Fe/H]$_{\rm LTE}$ values of 4936/1.86/−2.90, while Jacobson et al. (2015) list 4855/1.55/−3.02. Similarly, for SMSS J034249.52–284215.8 we find 4783/1.58/−2.31 compared

to 4828/1.60/−2.33 in Jacobson et al. (2015). The differences in the parameters are reassuringly low giving confidence that the results derived here can be straightforwardly compared with those of Jacobson et al. (2015). We also note that for star SMSS J221334.13–072604.1, Aoki et al. (2013) list parameters of 5150/1.8/−2.55 while we find 4810/1.52/−2.89; the higher abundance given by Aoki et al. (2013) is likely largely a direct consequence of the more than 300 K higher temperature employed in that study. For completeness, we note that Aoki et al. (2013) did not determine spectroscopic temperatures, rather they used the temperatures determined by the SEGUE Stellar Parameter Pipeline (SSPP) from the SEGUE low-resolution spectra (see Lee et al. 2011 and references therein). For this particular star, however, the temperature estimates given (but not used) by Aoki et al. (2013) from the $(V − K)_0$ and $(g − r)_0$ colours, namely 4724 K and 4867 K, are much more consistent with our determination of 4810 K than the SSPP value used by Aoki et al. (2013).

For completeness we also show in the bottom panel of Fig. 2 a comparison between the [Fe/H]$_{2.3m}$ values estimated from the fits to the low-resolution spectra and the final [Fe/H]$_{\rm LTE}$ values determined from the analysis of the high-resolution Keck spectra. Given that the low-resolution values are quantized at the 0.25 dex level, the agreement is reasonable: the mean difference is 0.33 dex, with the low-resolution estimates being lower, and the standard deviation of the differences is 0.32 dex.

In the following estimates of the internal uncertainties in chemical abundances due to the adopted model atmospheres will be estimated by varying the stellar parameters, one at a time, by $T_{\rm eff}$/log g/[M/H]/$\xi_t = ±100\,{\rm K}/±0.40\,{\rm cgs}/±0.30\,{\rm dex}/±0.40\,{\rm km\,s^{-1}}$.

3.2 Chemical species analysed

A list of the spectral lines used in the abundance analysis, together with the excitational potentials (E.P.), the total oscillator strengths (log gf) employed, and the measured EWs, is provided in Table 3. The atomic data come from Jacobson et al. (2015), with the exception of a few lines highlighted in Table 3. In most cases the analysis is based on the measurement of EWs via Gaussian fits to the profiles of well-isolated lines, as described in Marino et al. (2008); exceptions to this approach are discussed below. When required, and

Table 6. Chemical abundances for Fe I and Fe II, and Fe-peak elements Sc (Sc II), Cr, Mn, Co, Ni, and Zn. For each element we report the number (#) of analysed spectral features and the resulting rms (σ).

ID	[Fe/H]	σ	#	[FeII/H]	σ	#	[Sc/Fe]	σ	#	[CrI/Fe]	σ	#	[CrII/Fe]	#	[Mn/Fe]	σ	#	[Co/Fe]	σ	#	[Ni/Fe]	σ	#	[Zn/Fe]	σ	#
SMSS J202059.17−043447.0	−2.30	0.17	38	−2.36	0.35	4	0.13	0.35	4	−0.19	0.09	6	0.13	1	−0.25	0.03	3	+0.10	0.16	6	−0.02	–	1	0.06	0.02	2
SMSS J202400.03−024445.9	−1.97	0.19	36	−1.81	0.32	4	0.27	0.32	4	−0.20	0.11	6	−0.01	1	−0.78	0.21	3	+0.28	0.29	6	−0.21	0.01	2	0.29	0.11	2
SMSS J202601.44−033002.5	−2.84	0.15	27	−2.54	–	2	0.00	–	2	0.09	0.20	2	–	–	−0.56	0.18	3	+0.36	0.23	6	–	–	–	0.47	–	1
SMSS J202659.41−031149.2	−2.94	0.14	30	−2.84	–	2	0.41	0.46	2	−0.12	0.15	3	–	–	−0.84	0.03	3	+0.32	0.23	8	–	–	–	–	–	–
SMSS J204654.92−020409.2	−1.71	0.14	43	−1.61	0.46	4	0.10	–	4	−0.21	0.09	6	0.11	1	−0.74	0.08	3	+0.20	0.24	6	−0.20	0.10	8	0.01	0.01	2
SMSS J211657.83−012517.5	−2.56	0.15	29	−2.42	–	2	–	–	–	−0.04	0.16	4	0.17	1	−0.57	0.16	3	+0.21	0.35	5	0.18	–	1	–	–	1
SMSS J212001.71−001158.6	−2.58	0.16	38	−2.48	0.23	4	0.29	0.23	4	−0.23	0.11	5	0.24	1	−0.56	0.04	3	+0.21	0.37	4	−0.17	–	–	0.42	0.03	2
SMSS J212113.63−005132.2	−2.75	0.21	35	−2.50	–	2	0.02	–	2	−0.08	0.31	3	–	–	−0.57	0.17	3	−0.11	0.15	4	–	–	–	0.45	0.07	2
SMSS J212217.52−295552.7	−2.81	0.14	10	−2.62	–	1	–	–	–	–	–	1	–	–	−0.55	0.11	3	–	–	–	–	–	–	–	–	–
SMSS J220514.10−013407.6	−2.07	0.15	43	−2.02	0.43	4	0.29	0.43	4	−0.15	0.03	6	0.22	1	−0.58	0.21	3	+0.45	0.11	4	0.06	0.14	6	0.22	0.07	2
SMSS J220535.05−004403.6	−3.10	0.18	29	−3.06	0.40	2	0.34	0.40	2	−0.20	0.11	2	–	–	−0.44	0.11	3	+0.12	0.07	5	–	–	–	–	–	–
SMSS J221334.13−072604.1	−2.89	0.15	24	−2.80	–	1	–	–	–	−0.10	0.13	2	–	–	−0.69	0.15	3	+0.19	0.29	7	–	–	–	0.59	–	1
SMSS J222349.48−114751.1	−3.15	0.16	21	–	–	–	–	–	–	−0.28	–	1	–	–	−1.13	0.09	3	+0.16	0.19	7	–	–	–	–	–	–
SMSS J225336.83−270435.4	−3.26	0.19	8	–	–	1	–	–	–	–	–	–	–	–	−1.05	0.04	3	+0.18	0.36	4	–	–	–	–	–	–
SMSS J230306.22−041621.8	−2.74	0.16	32	−2.53	–	1	−0.14	–	1	−0.17	0.03	2	–	–	−0.54	0.05	3	+0.28	0.12	7	–	–	–	0.38	–	1
SMSS J010839.58−285701.5	−2.90	0.13	33	−2.91	–	1	–	–	1	−0.20	0.03	2	–	–	−0.59	0.16	3	+0.24	0.22	9	–	–	–	0.57	0.00	2
SMSS J034249.52−284215.8	−2.31	0.13	42	−2.21	0.06	4	−0.41	–	4	−0.31	0.11	6	0.19	1	−0.62	0.05	3	−0.35	0.20	8	−0.17	0.10	3	–	–	–

when atomic data are available from the literature, hyperfine and/or isotopic splitting was incorporated in the analysis, as indicated in the last column of Table 3.

We now comment in detail on the transitions used in the analyses for different element classes, noting that for some species abundances are determined only for a subset of the sample depending on the S/N of the spectrum and the adopted atmospheric parameters.

3.2.1 Light elements

Carbon abundances were derived via spectral synthesis of the CH *G*-band ($A^2\Delta - X^2\Pi$) heads near 4312 and 4323 Å. An oxygen abundance ratio of [O/Fe] = +0.4 dex was assumed as the S/N of the spectra does not allow a determination of the oxygen abundance from the forbidden [O I] lines at 6300 and 6363 Å. Examples of the synthetic spectrum fits are shown in the left-hand panels of Fig. 3. Similarly, nitrogen abundances come from spectral synthesis of the CN bands $B^2\Sigma - X^2\Sigma$ at ∼3880 and ∼4215 Å, using the carbon abundance derived from the *G*-band fits. Sodium abundances were inferred from the Na resonance doublet at ∼5893 Å. For three stars we were able to estimate Na from the doublet ∼5685 Å. Sodium abundances were then corrected for non-LTE effects, as in Lind et al. (2011), and listed in Table 4. For most stars, we were able to infer Al abundances from the spectral synthesis of the lines used also in Jacobson et al. (2015), namely at ∼3961 and ∼3944 Å.

3.2.2 α-Elements

We determined chemical abundances for the α-elements Mg, Si, Ca, and Ti. For magnesium, silicon, and titanium the abundances could be determined for all the stars in the observed sample, since at least one up to three strong lines were available for these elements; a larger number of lines were generally detectable for Ti, particularly for Ti II. Calcium abundances were inferred from only one or two lines (see Table 5).

3.2.3 Iron-peak elements

A few lines were available for each of the iron-peak elements Sc, Cr, Mn, Co, Ni, and Zn (see Table 6). The abundances for these elements were determined from the measured EWs except for Mn where we synthesized the triplet at ≈4033 Å to take into account hyperfine structure.

3.2.4 Neutron-capture elements

We derived abundances for the neutron-capture elements Sr (from the resonance lines 4078,4215 Å), Ba (from the resonance lines 4554,4934 Å, and the spectral feature 5854 Å), and Eu (from the resonance line 4130 Å). Specifically, we employed a spectrum synthesis approach to the analysis since hyperfine and/or isotopic splitting and/or blended features needed to be taken into account. For example, the spectral features of Eu II have both significant hyperfine substructure and isotopic splitting. For this element Solar system, isotopic fractions were assumed in the computation. The right-hand panels of Fig. 3 show examples of the synthetic spectrum fits to the strong Ba II line at 4934.1 Å. Our Ba abundances were computed assuming the McWilliam (1998) r-process isotopic composition and hyperfine splitting. The derived abundances are listed in Table 7.

Table 7. Chemical abundances for the *n*-capture elements, Sr, Ba, and Eu. For each element we report the number (#) of analysed spectral features and the resulting rms (σ). For some stars we report upper limits.

ID	[Sr/Fe]	σ	#	[Ba/Fe]	σ	#	[Eu/Fe]	σ	#
SMSS J202059.17–043447.0	0.12	0.08	2	− 0.42	0.13	3	− 0.07	–	1
SMSS J202400.03–024445.9	0.20	0.29	2	0.05	0.04	3	0.68	0.03	2
SMSS J202601.44–033002.5	0.20	0.04	2	− 0.41	0.10	2	<0.80	–	–
SMSS J202659.41–031149.2	− 1.94	0.06	2	− 1.69	0.00	1	<0.10	–	–
SMSS J204654.92–020409.2	0.03	0.00	2	− 0.13	0.16	3	0.35	0.19	2
SMSS J211657.83–012517.5	− 0.18	0.21	2	− 0.41	0.09	3	0.28	–	1
SMSS J212001.71–001158.6	− 0.41	0.07	2	− 0.82	0.15	3	− 0.28	–	1
SMSS J212113.63–005132.2	− 0.51	0.01	2	− 1.00	0.02	2	<0.20	–	–
SMSS J212217.52–295552.7	− 1.15	0.05	2	< − 0.90	0.10	2	<0.80	–	–
SMSS J220514.10–013407.6	0.03	0.07	2	− 0.38	0.10	3	0.05	–	1
SMSS J220535.05–004403.6	− 0.82	0.03	2	− 1.45	0.09	2	<0.30	–	–
SMSS J221334.13–072604.1	− 0.36	0.04	2	− 1.00	0.09	2	<0.30	–	–
SMSS J222349.48–114751.1	− 2.00	0.10	2	− 1.63	0.02	2	<0.20	–	–
SMSS J225336.83–270435.4	− 0.61	0.10	2	− 1.12	0.15	2	<0.90	–	–
SMSS J230306.22–041621.8	− 0.01	0.01	2	− 0.58	0.10	3	<0.30	–	–
SMSS J010839.58–285701.5	0.07	0.01	2	− 0.41	0.11	2	<0.30	–	–
SMSS J034249.52–284215.8	− 0.10	0.01	2	− 0.14	0.10	3	0.55	0.01	2

Table 8. Sensitivity of derived abundances to the uncertainties in atmospheric parameters, the limilted S/N ($\sigma_{S/N}$), and the total error due to these contributions (σ_{tot}).

	ΔT_{eff} ±100 K	$\Delta \log g$ ±0.40	$\Delta \xi_t$ ±0.40 km s^{-1}	Δ[A/H] 0.30 dex	$\sigma_{S/N}$	σ_{total}
[C/Fe]	±0.09	−0.10	±0.05	±0.11	0.14	0.23
[N/Fe]	±0.16	−0.08	±0.06	−0.20	0.14	0.31
[Na/Fe]	±0.01	−0.05	−0.10	−0.01	0.14	0.18
[Mg/Fe]	−0.06	−0.01	±0.02	±0.01	0.14	0.15
[Al/Fe]	±0.01	−0.12	−0.10	±0.03	0.35	0.38
[Si/Fe]	−0.01	−0.05	−0.03	±0.01	0.33	0.34
[Ca/Fe]	−0.05	±0.01	±0.04	±0.01	0.14	0.15
[Ti I/Fe]	±0.02	±0.00	±0.05	±0.00	0.10	0.11
[Ti II/Fe]	±0.04	−0.01	−0.08	±0.00	0.08	0.12
[Fe I/H]	±0.12	−0.03	−0.08	−0.02	0.04	0.15
[Fe II/H]	−0.00	±0.12	−0.03	±0.02	0.14	0.19
[Sc/Fe]	±0.02	−0.04	±0.01	±0.00	0.33	0.33
[Cr I/Fe]	−0.01	±0.00	±0.05	±0.01	0.16	0.17
[Cr II/Fe]	−0.01	−0.07	±0.02	−0.01	0.20	0.21
[Mn/Fe]	±0.06	−0.07	−0.08	−0.13	0.12	0.21
[Co/Fe]	±0.02	−0.03	−0.07	−0.01	0.17	0.19
[Ni/Fe]	−0.06	±0.03	±0.08	±0.01	0.12	0.16
[Zn/Fe]	−0.09	±0.07	±0.07	±0.02	0.14	0.19
[Sr/Fe]	±0.07	−0.06	−0.22	−0.04	0.14	0.30
[Ba/Fe]	±0.07	−0.02	−0.05	−0.02	0.14	0.30
[Eu/Fe]	±0.05	±0.01	±0.03	±0.06	0.20	0.22

3.2.5 Abundance errors

Estimates of the uncertainties in the chemical abundances due to errors in the atmospheric parameteres have been obtained by rerunning the abundances, one at a time, varying T_{eff}/log g/[m/H]/ξ_t by ±100 K/±0.40/±0.30/±0.40 km s^{-1}, assuming that the errors are symmetric for positive and negative changes. The uncertainties used in T_{eff}, log g, and [m/H] are reasonable, as suggested by the comparison with the spectrophotometric fits to the 2.3 m low-resolution spectra and stars in common with Jacobson et al. (2015) (see Section 3.1). As internal errors in ξ_t, we conservatively adopt ±0.40 km s^{-1}. The variations in chemical abundances for each element are listed in Table 8.

To obtain the total error estimates, we follow the approach by Norris et al. (2010) and Yong et al. (2013). For each element, we replace the r.m.s (σ) in Tables 4, 5, 6, and 7 by the maximum(σ, 0.20), where the second term is what would be expected for a set of N lines (N_{lines}) with a dispersion of 0.20 dex (a conservative value for the abundance dispersion of Fe I lines as listed in Table 6). Then, we derive max(σ, 0.20)/$\sqrt{N_{lines}}$. Typical values obtained for each element are listed in column (6) of Table 8. The total error is obtained by quadratically adding this random error with the uncertainties introduced by atmospheric parameters. For Sr and Ba we conservatively adopt an uncertainty of 0.30 dex, considering that the abundances for these elements mostly come from strong
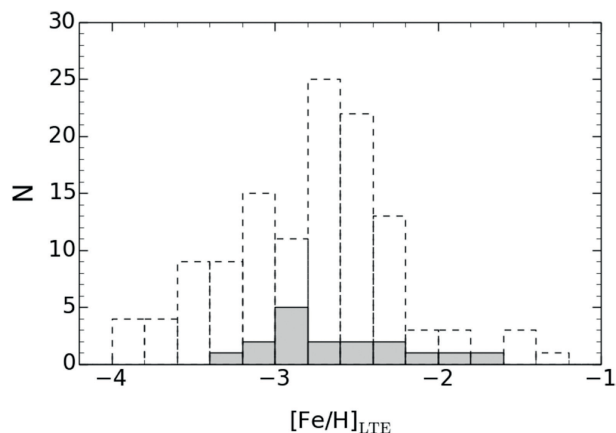
Figure 4. Distribution of the [Fe/H]$_{\rm LTE}$ abundances of our analysed stars (filled-grey histogram) and of the larger sample analysed in Jacobson et al. (2015) (dashed-empty histogram).

resonance lines. Finally, we note that this 1D LTE analysis is subject to abundance uncertainties from three-dimensional (3D) and non-LTE effects (Asplund 2005).

4 RESULTS

The distribution of [Fe/H]$_{\rm LTE}$ for the sample of 17 commissioning-era SkyMapper EMP candidates observed at Keck is shown in Fig. 4, where it is compared with the [Fe/H]$_{\rm LTE}$ distribution for the larger sample of 122 commissioning-era SkyMapper EMP candidates observed at Magellan and analysed in Jacobson et al. (2015). In the Jacobson et al. (2015) sample, one-third of the stars have [Fe/H]$_{\rm LTE}$ < −3.0, while 43 per cent have [Fe/H]$_{\rm LTE}$ <−2.8 dex. Given the smaller size, the current sample is fully consistent with these fractions as ∼20 per cent (3/17) of the stars are found here to have [Fe/H]$_{\rm LTE}$ <−3.0 dex and 47 per cent (8/17) have [Fe/H]$_{\rm LTE}$ <−2.8 dex. The SkyMapper photometric selection technique is therefore clearly quite efficient in selecting metal-poor stars. Indeed, as noted above, using the SkyMapper DR1.1

photometry, ∼40 per cent of the candidates that fall within the selection window shown in Fig. 1, have [Fe/H]$_{2.3m}$ ≤ −2.75 dex. As a comparison, the similar Northern hemisphere photometric survey for EMP stars, *Pristine*, finds that ∼24 per cent of candidates photometrically selected to have [Fe/H] < −3.0 have spectroscopically determined abundances below [Fe/H] = −3.0 dex (Starkenburg et al. 2017). As in Jacobson et al. (2015), we caution against using the commissioning-era results to constrain the metallicity distribution function at low abundances, as the selection biases cannot be reliably established. Future papers based on a much larger sample of stars selected from SkyMapper DR1.1 photometry and observed at low resolution, coupled with an extensive follow-up investigation with Magellan, will, however, address this issue.

In the following subsections we consider the abundance trends among and between elements of different nucleosynthetic groups. We use as our comparison samples those of Jacobson et al. (2015) and the giant stars in the compilation of Yong et al. (2013), noting that the parameter determination approaches and the line-lists in those works are not identical to those used here so that the possibility of systematic differences cannot be ruled out. Unless otherwise noted, all abundances and abundance ratios are 1D LTE values.

4.1 Light elements

4.1.1 Carbon

As a star ascends the red giant branch, the envelope expands inwards, reaching layers affected by CN-cycling, a consequence of which is a reduction of the carbon abundance in the surface layers (and an increase in the surface abundance of N). Since we are interested in the carbon abundance at the star's birth, the so-called 'natal' abundance, our measured carbon abundances need to be corrected for the effects of this evolutionary mixing. The evolutionary mixing corrections depend on $T_{\rm eff}$, log g, and [Fe/H] and have been discussed in detail in Placco et al. (2014). Dr. V. Placco (Placco, 2018, private communication) kindly generated the appropriate corrections to our observed carbon abundances by assuming a natal [N/Fe] = +0.0 and applying the Placco et al. (2014) procedure. Table 4 lists the observed [C/Fe] values and the
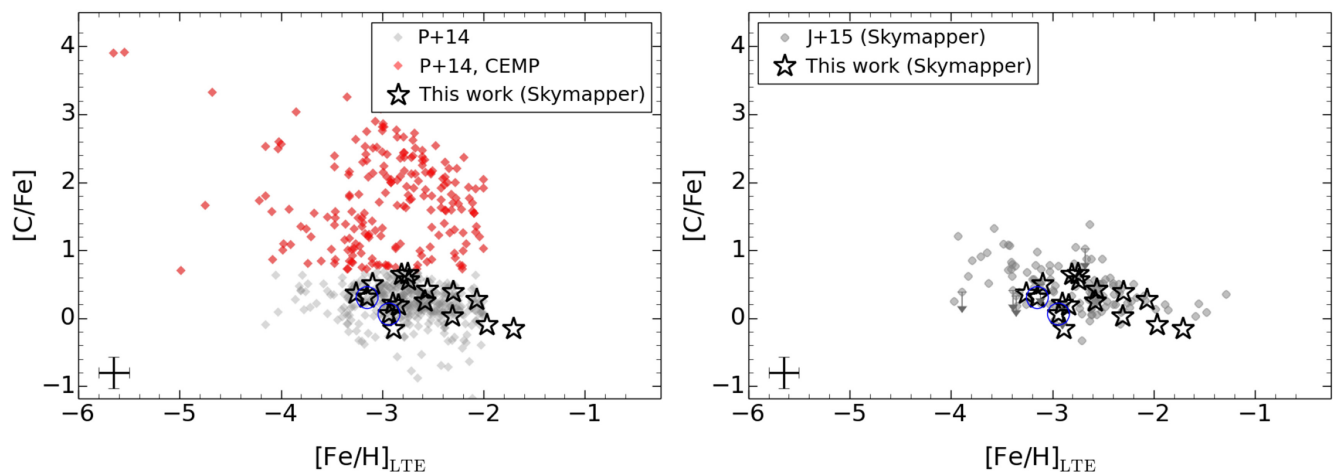
Figure 5. [C/Fe], corrected for evolutionary mixing effects, as a function of [Fe/H]$_{\rm LTE}$ for our sample of stars, which are shown as black open 5-pointed star symbols. The left-hand panel shows the comparison of our observed values with the compilation of Placco et al. (2014), shown as grey- and red-filled diamonds with the latter marking CEMP stars. In the right-hand panel we compare our evolutionary-mixing corrected values with those of Jacobson et al. (2015), plotted as grey-filled circles, that are also corrected for evolutionary-mixing effects. The two stars indicated with blue open circles are the stars with low neutron-capture elements, as will be discussed in Section 4.4.1.
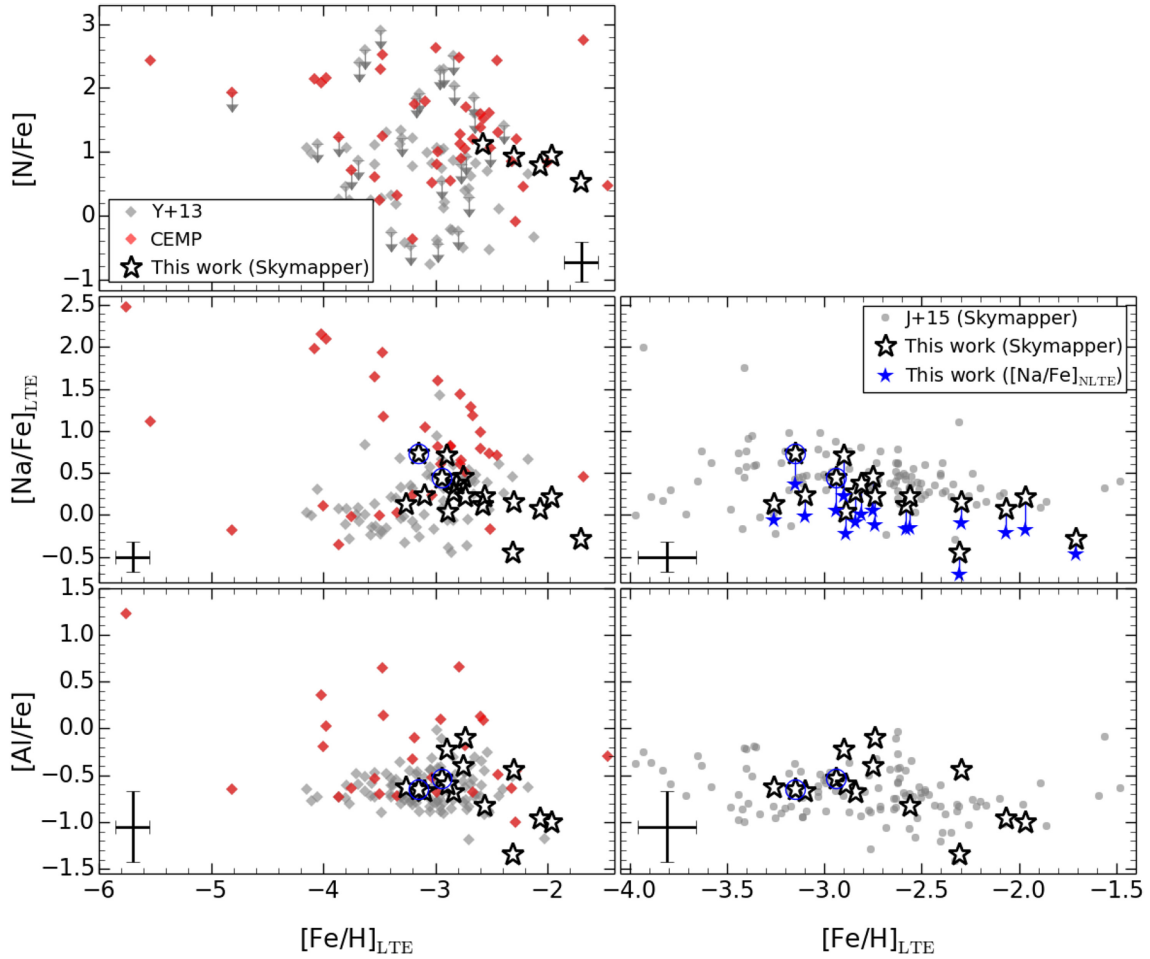
Figure 6. Nitrogen, sodium, and aluminum abundance ratios, relative to iron, as a function of [Fe/H]$_{LTE}$. The [N/Fe] abundances are compared with the sample of Yong et al. (2013) in the upper-left panel where upper limits on the [N/Fe] values are shown as downward-pointing arrows. The LTE [Na/Fe] abundance ratios derived here are compared with the Yong et al. (2013) values in the middle-left panel (symbols as for the upper-left panel), and with the Jacobson et al. (2015) sample in the middle-right panel. In the middle-right panel we also show, as blue-filled stars, our [Na/Fe] values corrected for non-LTE (NLTE) effects. These lie at lower values and are connected to the corresponding LTE points by thin blue lines. Aluminum abundances are compared with the Yong et al. (2013) and the Jacobson et al. (2015) in the lower-left and lower-right panels, respectively. The two stars indicated with blue open circles are the stars with low neutron-capture elements, as will be discussed in Section 4.4.1.

correction for evolutionary mixing: the estimated 'natal' [C/Fe] is formed by adding the correction to the observed value.

In Fig. 5 we show in the left-hand panel a comparison of our observed [C/Fe] values with those listed in Placco et al. (2014), which are corrected for evolutionary-mixing effects. The right-hand panel shows the comparison of our [C/Fe] values, after applying the evolutionary mixing corrections, with the evolutionary mixing corrected values of Jacobson et al. (2015). Placco et al. (2014) have demonstrated that the fraction of carbon-enhanced metal-poor (CEMP) stars, defined as stars possessing [C/Fe] $\geq$ +0.7 dex, increases with decreasing metallicity with CEMP stars dominant below [Fe/H] $\leq$ −4.0 (see also Yoon et al. 2016, 2018). The Placco et al. (2014) CEMP frequencies (e.g. ~40 per cent for [Fe/H] $\leq$ −3.0) would suggest that our sample of three stars with [Fe/H]$_{LTE}$ $\leq$ −3.0 should contain one CEMP-star whereas there are none. While the statistical weight of the lack of CEMP-stars compared to the number expected is not high, inspection of Fig. 5 reveals that none of our sample of 17 stars has a [C/Fe] value that would cause it to be classified as CEMP-star: the highest evolutionary corrected [C/Fe] values are 0.66 dex for SMSS J212113.63−005132.2 ([Fe/H]$_{LTE}$ = −2.74) and 0.64 dex

for SMSS J212217.52−295552.7 ([Fe/H]$_{LTE}$ = −2.81). In general, our evolutionary mixing corrected [C/Fe] values are completely consistent with those from the larger sample of Jacobson et al. (2015). Jacobson et al. (2015) discussed the frequency of CEMP-stars in their sample and concluded that it is comparable with that of Placco et al. (2014) although, as is evident in Fig. 5, the Jacobson et al. (2015) sample lacks CEMP-stars with [C/Fe] significantly above 1.0.

The most likely explanation lies in the selection of EMP candidates from the SkyMapper photometry. As discussed in Da Costa et al. (), the strong *CH* bands in the spectrum of a CEMP-star can depress the flux in the SkyMapper *v*-filter sufficiently that the inferred metallicity index mimics a more metal-rich star, and thus decreases the probability that it will be selected for low-resolution spectroscopic follow-up. Nevertheless the commissioning survey did result in the discovery of the most iron-poor star currently known, a star that is extremely C-rich (Keller et al. 2014; Bessell et al. 2015; Nordlander et al. 2017). Evidently at sufficiently low overall abundance the contaminating carbon features in the *v* band weaken enough that selection as a photometric candidate again becomes possible.
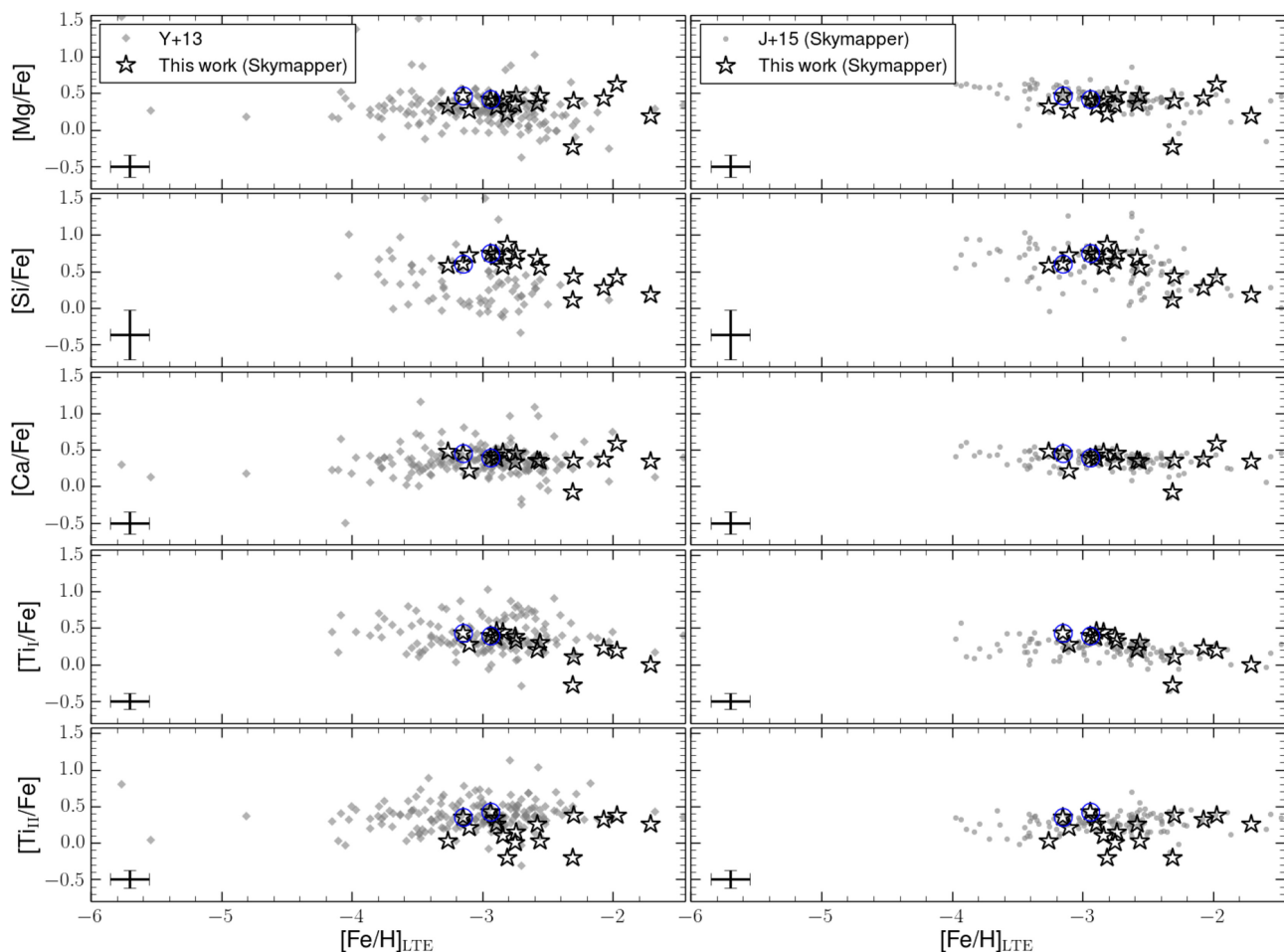
Figure 7. Chemical abundance ratios with respect to Fe for the α-elements measured in this study as a function of [Fe/H]$_{LTE}$. The 5-point star symbols are the stars in the current sample, while the grey solid circles are stars from Yong et al. (2013, left-hand panels) and Jacobson et al. (2015, right-hand panels). The two stars indicated with blue open circles are the stars with low neutron-capture elements, as will be discussed in Section 4.4.1.

4.1.2 Nitrogen, sodium, and aluminum

The nitrogen, sodium, and aluminum abundance ratios with respect to iron for our sample are shown in Fig. 6 as a function of [Fe/H]$_{LTE}$. Because of low S/N at the wavelength of the *CN* bands in many of the spectra, [N/Fe] values could be determined only for five stars in our sample. The values, which lie between 0.5 and ∼1.0, and which are listed in Table 4, are nevertheless consistent with the midpoint of the substantial range of [N/Fe] values found in the sample of Yong et al. (2013).

For sodium, while noting that the non-LTE corrections would result in lower abundance ratios, we have plotted the LTE abundance ratios to facilitate comparison with the Yong et al. (2013) and Jacobson et al. (2015) samples. In the comparison plot with Jacobson et al. (2015) we have also plotted our non-LTE-corrected values of Na (Lind et al. 2011), to highlight the general lower abundances for this element that would be obtained with a proper non-LTE analysis. It is clear from the panels of Fig. 6 that our results for [Na/Fe] are generally consistent with those of the earlier studies. The one possible exception is the star SMSS J034249.52–284215.8, which has [Na/Fe]$_{LTE}$ of −0.44 and [Fe/H]$_{LTE}$ = −2.31 dex. Such a low [Na/Fe] is reminiscent of the low [Na/Fe] values seen in red giant members of dwarf Spheroidal galaxies (e.g. Geisler et al.

2005; Hasselquist et al. 2017; Norris et al. 2017, and references therein). The low value for [Na/Fe] found here is consistent with that listed by Jacobson et al. (2015): [Na/Fe]$_{LTE}$ = −0.29, the lowest [Na/Fe]$_{LTE}$ in their entire sample. We give both the LTE and non-LTE [Na/Fe] values for our stars in Table 4.

Aluminum abundance ratios of our sample are comparable to both those of Yong et al. (2013) and Jacobson et al. (2015) (lower panels of Fig. 6). We note that the uncertainties associated with our [Al/Fe] values are large due to the relatively low S/N of our spectra, especially below 4000 Å. As for [Na/Fe] we expect the application of non-LTE corrections to generate systematic offsets in the [Al/Fe]$_{LTE}$ values; such corrections can be as large as +0.65 dex (Baumueller & Gehren 1997). As discussed in the previous work, such higher non-LTE [Al/Fe] abundances would be more consistent with predictions of chemical evolution models (e.g. Kobayashi et al. 2006).

4.2 α-Elements

The individual α-element (Mg, Si, Ca, Ti I, Ti II) abundances for our sample are displayed as a function of [Fe/H]$_{LTE}$ in Fig. 7 and listed in Table 5. With the exception of one star, all our stars are α-enhanced and their location in the [element/Fe] panels is fully consistent with the larger comparison samples of Jacobson et al. (2015) and Yong et al. (2013).
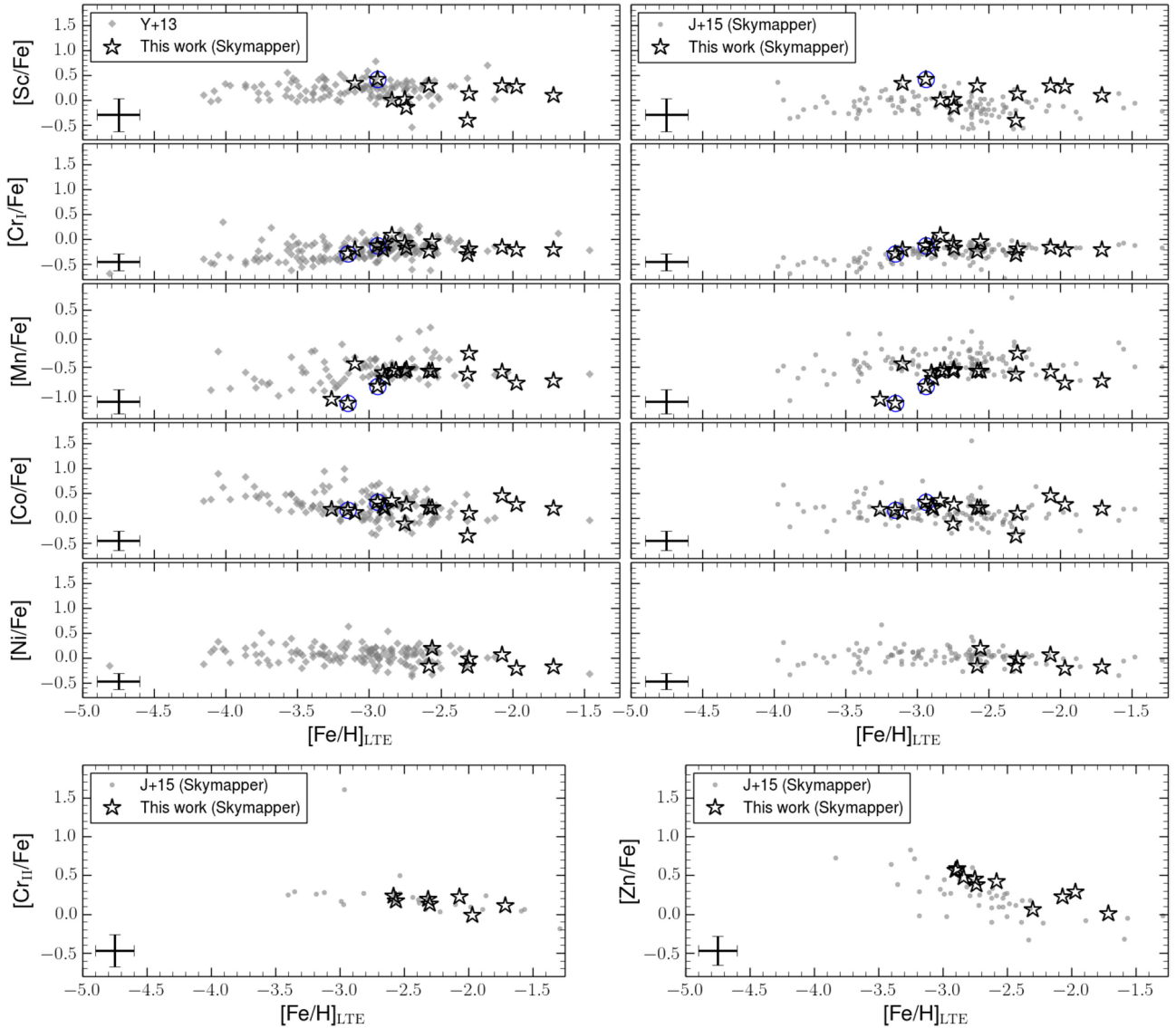
Figure 8. Chemical abundance ratios with respect to Fe for the iron-peak elements as a function of [Fe/H]$_{LTE}$. Symbols are as in Fig. 7. The left-hand panels show the comparison with the results of Yong et al. (2013), while the right-hand panels show the comparison with Jacobson et al. (2015). The two stars indicated with blue open circles are the stars with low neutron-capture elements, as will be discussed in Section 4.4.1.

The one star that does not show any α-enhancement is the star SMSS J034249.52–284215.8, which was identified as a 'Fe-enhanced' star in Jacobson et al. (2015, specifically Section 5.1). For this star we find ([Mg/Fe], [Si/Fe], [Ca/Fe], [Ti/Fe] I and [Ti/Fe] II) values of (−0.24, +0.11, −0.08, −0.28, −0.20), values that are fully consistent with those of Jacobson et al. (2015), which are (−0.17, +0.14, −0.16, −0.37, −0.13). We find also that the other elements analysed in this star generally have sub-solar ratios, again consistent with Jacobson et al. (2015). We note that in Section 3.1 we have used α-enhanced isochrones for all the stars. A solar-scaled [α/Fe] isochrone, more appropriate for this star, results in a lower log g by ∼0.10 dex, which does not significantly affect the derived abundances relative to Fe (see Table 8).

Discussion of the possible origin(s) of this star is given in Jacobson et al. (2015). We only note that as mentioned above, the low [Na/Fe] for this star, plus its 'alpha-poor' nature, is reminiscent of abundance ratios seen in dSph stars. The kinematics of the star are not unusual in comparison with those for the rest of the sample.

This star also has the lowest [Al/Fe] in both our sample and that of Jacobson et al. (2015).

4.3 Fe-peak elements

In Fig. 8 we show our results for the abundance ratios with respect to iron for the iron-peak elements Sc, Cr I, Cr II, Mn, Co, Ni, and Zn as a function of [Fe/H]$_{LTE}$. The values are listed in Table 6 along with both the number of spectral features analysed and the standard deviations (σ). Also shown in the panels are the equivalent data, where available, for the stars in the comparison samples of Yong et al. (2013) and Jacobson et al. (2015). Although our sample is not large compared to the others, it is evident from the figure that our results are consistent with the abundance ratio trends seen in the comparison samples. There is, however, a suggestion that the Keck data presented here have some systematic differences relative to the comparison samples. For example, although the Keck stars show the same rate of increase in [Zn/Fe] with decreasing [Fe/H]$_{LTE}$ as the
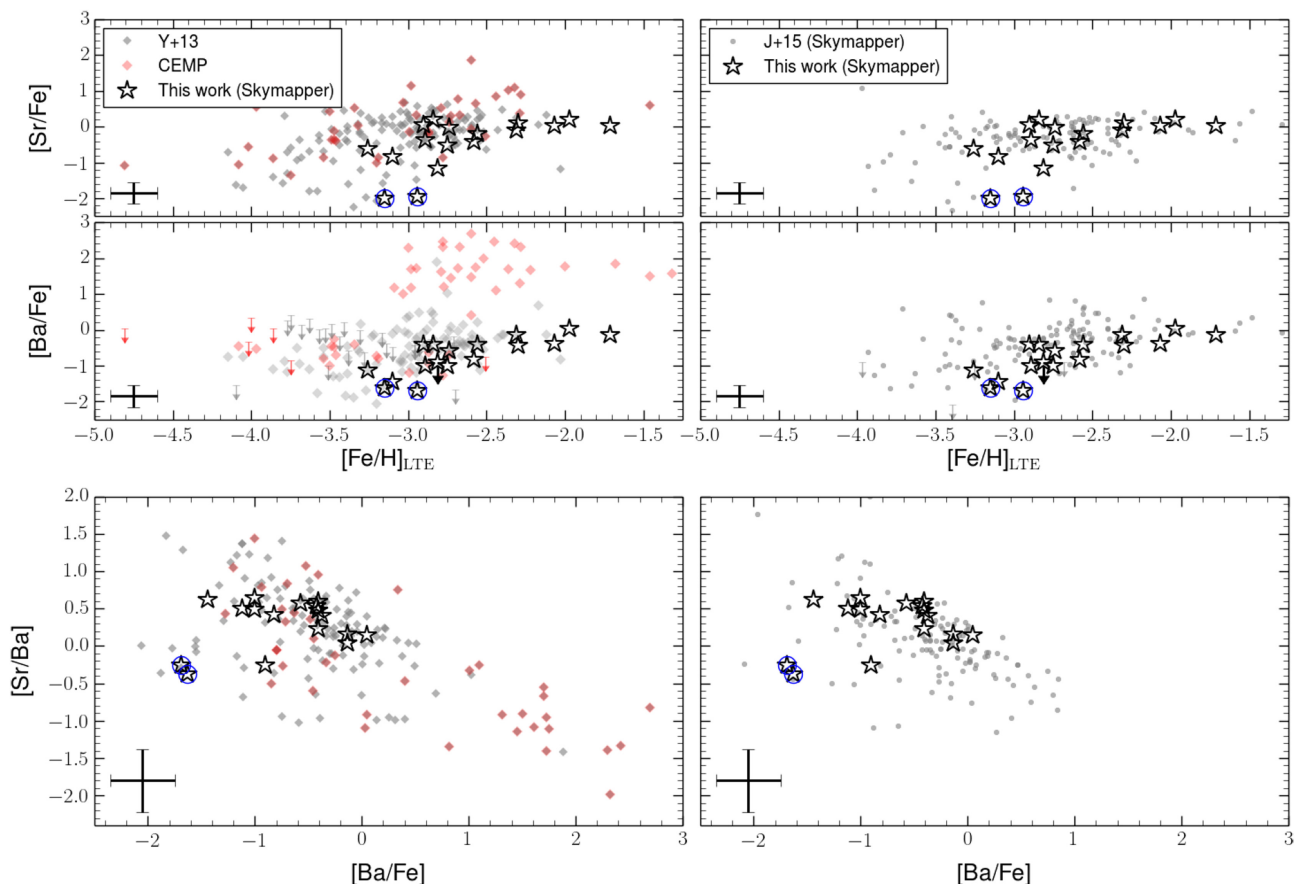
Figure 9. *Upper panels:* Chemical abundance ratios with respect to Fe for the neutron-capture elements Sr and Ba as a function of [Fe/H]$_{\rm LTE}$. *Lower panels:* [Sr/Ba] as a function of [Ba/Fe]. We compare our results with data from Yong et al. (2013) in the left-hand panels and with Jacobson et al. (2015) in the right-hand panels. Symbols are as in Fig. 5. The two stars indicated with blue open circles are the stars with low neutron-capture elements.

stars in the Jacobson et al. (2015) sample, there might be an offset in that the current sample have [Zn/Fe] abundance ratios ∼0.2 dex higher than the Jacobson et al. (2015) values at similar [Fe/H]. The star observed here that is in common with Jacobson et al. (2015) is consistent with this offset.

4.4 *n*-Capture elements

4.4.1 *Strontium and barium*

Among the *n*-capture elements, those that could be analysed in the spectra of the majority of the stars observed here are Sr and Ba. As regards the s-process, Sr is a first s-process peak element while Ba occurs in the second s-process peak. Both can be generated by the ^{22}Ne or the ^{13}C neutron source depending on the neutron exposure. These elements can also have r-process contributions and thus the relative abundances of these elements in metal-poor stars can provide information on nucleosynthetic processes at early times.

The abundance ratios [Sr/Fe] and [Ba/Fe] for the stars in our sample are shown as a function of [Fe/H]$_{\rm LTE}$ in the upper and middle panels of Fig. 9 and are listed in Table 7. We note first that none of our stars show high (>1 dex) abundance ratios for these elements, i.e. none can be classified as *s*-enhanced stars. This is consistent with the lack of CEMP-stars in our sample, as discussed in Section 4.1. As is also apparent in the panels of Fig. 9, our results are generally consistent with those of Yong et al. (2013), which include CEMP-*s* stars, and Jacobson et al. (2015). There is some indication that

perhaps our [Sr/Fe] values are systemically lower than those of Jacobson et al. (2015), by approximately 0.3 dex, which is however within our observational uncertainties (see Table 8).

It is well-known that as overall abundance decreases, the dispersion in the abundance ratios for the *n*-capture elements relative to iron increases markedly (e.g. McWilliam et al. 1995; Frebel & Norris 2015, and references therein), undoubtedly reflecting variations in the relative contributions of the numerous nucleosynthetic origins for these elements. This is illustrated in the lower panels of Fig. 9, where we show the [Sr/Ba] ratio as a function of [Ba/Fe], including CEMP-*s* stars. Concentrating on the stars without *s*-enhancements, i.e. those with [Ba/Fe] ≤ 0.0 approximately, we see that the range in [Sr/Ba] increases substantially as [Ba/Fe] decreases reaching almost two orders of magnitude at the lowest [Ba/Fe] values. The data suggest that the upper limit on [Sr/Ba] increases as [Ba/Fe] decreases, whereas the lower limit appears approximately constant with decreasing [Ba/Fe]. The Solar system r-process pattern has [Sr/Ba] = −0.5 dex, though lower values are seen in some ultra-faint dwarf galaxy member stars (see Frebel & Norris 2015 and references therein) and do occur in both the Yong et al. (2013) and Jacobson et al. (2015) data sets.

Casey & Schlaufman (2017) found a star with [Ba/Fe] ∼ −3, with typical main r-process abundance patterns, a signature of the universality of the r-process. Six stars with very low [Ba/Fe] ([Ba/Fe]<−1.5) but which show a range of [Sr/Ba] of ∼2 dex were identified by Jacobson et al. (2015). One of these stars has [Sr/Ba] ≈ −0.5, i.e. the Solar system r-process value, with an upper
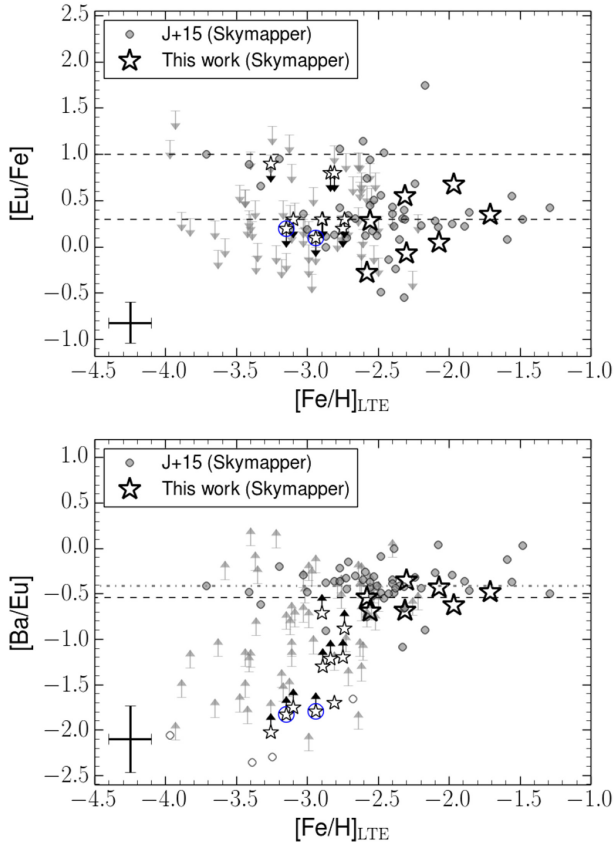
Figure 10. *Upper panel*: [Eu/Fe] as a function of [Fe/H]$_{LTE}$ for our sample compared with the Jacobson et al. (2015) sample. In both cases upper limits on [Eu/Fe] are indicated by downward pointing arrows. The dashed lines are [Eu/Fe] = +0.3 and [Eu/Fe] = +1 show the classification values for *r*-I and *r*-II stars, respectively. The two stars indicated with blue open circles are the two stars with the lowest neutron-capture element abundances. *Lower panel*: [Ba/Eu] as a function of [Fe/H]$_{LTE}$ for the stars with measured Eu abundances or upper limits. Symbols are as in the upper panel. The four open circles in the Jacobson et al. (2015) sample are the stars with upper limits in both Ba and Eu. One star in our sample also has only upper limits and has been represented with a small star-like symbol, without upward limit. The black dashed line and the grey dotted-dashed line are the mean [Ba/Eu] abundances in our sample and Jacobson et al. (2015), respectively. The size of the *y*-axis has been kept the same as in the upper panel.

limit on [Eu/Fe] of ∼0.4 dex. It is therefore strongly depleted in *n*-capture elements. We have identified two similar stars in our sample: SMSS J202659.41–031149.2 for which [Fe/H]$_{LTE}$ = −2.94, [Ba/Fe] = −1.69 and [Sr/Ba] = −0.25, and SMSS J222349.48–114751.1 for which the corresponding values are −3.15, −1.63, and −0.37 dex. Neither star has a detectable Eu II line at 4129 Å yielding an approximate upper limit of [Eu/Fe] ≈ 0.10–0.20 dex. Detailed abundances for other *n*-capture elements for these stars would provide important information on *n*-capture nucleosynthesis processes at early times, e.g. the weak r-process versus the main r-process (e.g. Roederer 2013; Li et al. 2015b).

4.4.2 Europium

Europium is predominantly synthesized by the r-process (e.g. Sneden, Cowan & Gallino 2008) and as such, the [Eu/Fe] abundance ratio is used to identify r-processed enhanced stars: *r*-II stars have [Eu/Fe] ≥ +1.0 while the more moderately enhanced *r*-I stars have 0.3 ≤ [Eu/Fe] ≤ 1.0 dex. Both types have [Ba/Eu] < 0 (Barklem

et al. 2005). We have measured Eu abundances for as many of the stars in our sample as possible, and derived upper limits for the others. The results are shown in the upper panel of Fig. 10, where we compare our results with those of Jacobson et al. (2015) (we note that Yong et al. 2013 did not determine Eu abundances). The agreement is reasonable. The [Eu/Fe] determinations are also given in Table 7. Overall, the scatter in the [Eu/Fe] values is comparable to that seen in Jacobson et al. (2015) and to that in the literature compilation of Frebel (2010). One star in our sample, SMSS J202400.03–024445.9, is a probable *r*-I star – for this star, which has [Fe/H]$_{LTE}$ = −1.95, we find [Eu/Fe] = +0.68 and [Ba/Eu] = −0.63 dex. Star SMSS J034249.52–284215.8, which we have already drawn attention to because of its low values of [α/Fe] and [Na/Fe], and which is the 'Fe-enhanced' star discussed in Jacobson et al. (2015), is also a candidate *r*-I star. It has [Fe/H]$_{LTE}$ = −2.31, [Eu/Fe] = +0.55, and [Ba/Eu] = −0.67 dex. Star SMSS J204654.92–020409.2 also just meets the *r*-I classification with [Fe/H]$_{LTE}$ = −1.70, [Eu/Fe] = +0.35, and [Ba/Eu] = −0.48 dex. Indeed the [Ba/Eu] abundance ratio in all three stars is consistent with the scaled-solar r-process value. The lower panel of Fig. 10 shows the abundance ratio [Ba/Eu] as a function of [Fe/H]$_{LTE}$. The average [Ba/Eu] for all the seven stars with both Ba and Eu measurements is −0.54, close to the scaled-solar r-process value. We note that for these stars, the standard deviations of the [Ba/Fe] and [Eu/Fe] values are 0.28 and 0.34 dex, respectively. However, the standard deviation of the [Ba/Eu] ratio for these stars is substantially less at 0.13 dex. This may indicate that while the total production of Ba and Eu is variable, the nucleosynthetic site(s) involved produce Ba and Eu in very similar relative amounts.

5 SUMMARY

We have presented here the results of an analysis of high-resolution spectra, obtained with the Keck telescope and the HIRES spectrograph, of 17 candidate EMP stars selected from SkyMapper commissioning-era photometry. Fourteen of the stars had not previously been observed at high dispersion. We find that, as in Jacobson et al. (2015), the candidate selection process, i.e. photometry plus low-resolution spectroscopy, is robust with almost half of the sample having [Fe/H]$_{LTE}$ ≤ −2.8 and with only one 'false positive' – an EMP candidate for which [Fe/H] turned out to exceed [Fe/H]$_{LTE}$ = −2.0 dex. In general, the distribution of element abundances and abundance ratios for this sample closely mimics the earlier results of Jacobson et al. (2015) that was based on Magellan/MIKE high-dispersion spectroscopy of a large sample of SkyMapper commissioning-era EMP candidates. Specifically, we find that none of the present sample can be classified as CEMP stars. Further, we confirm the results of Jacobson et al. (2015) that the star SMSS J034249.52–284215.8 is an example of the relatively rare class of objects known as 'Fe-enhanced' stars – stars with generally sub-solar abundance ratios, including for the α-elements. The star may have originated in a dwarf spheriodal galaxy. Two further stars, SMSS J202659.41–031149.2 and SMSS J222349.48–114751.1, are found to be strongly depleted in *n*-capture elements: [Ba/Fe]<−1.6, [Sr/Ba] ≈ −0.3 dex, and [Eu/Fe] ≲ +0.10–0.15 joining the similar star identified in Jacobson et al. (2015), while the star SMSS J202400.03–024445.9 is a probable *r*-I star with [Eu/Fe] = +0.68, [Ba/Eu] = −0.63, and [Fe/H]$_{LTE}$ = −1.95 dex.

ACKNOWLEDGEMENTS

We thank the anonymous referee for his or her suggestions that improved the manuscript. We thank Dr Vini Placco for providing the

evolutionary mixing corrections to the observed carbon abundances. SkyMapper research on EMP stars has been supported in part through the Australian Research Council (ARC) Discovery Grant programs DP120101237 and DP150103294 (Lead-CI Da Costa). A. F. M., A. R. C., and A. D. M. have been in part supported by ARC through the Discovery Early Career Researcher Award DE160100851, the Discovery Project DP160100637, and the Future Fellowship FT160100206, respectively. M. A. gratefully acknowledges generous funding from an ARC Laureate Fellowship (grant FL110100012). Parts of this research were conducted under the auspices of the Australian Research Council Centre of Excellence for All Sky Astrophysics in 3 Dimensions (ASTRO 3D), which is supported through project number CE170100013. This project has received funding from the European Union's Horizon 2020 research and innovation programme under the Marie Skłodowska-Curie Grant Agreement No. (797100; Beneficiary: A. F. M.).

The national facility capability for SkyMapper has been funded through ARC LIEF grant LE130100104 from the Australian Research Council, awarded to the University of Sydney, the Australian National University, Swinburne University of Technology, the University of Queensland, the University of Western Australia, the University of Melbourne, Curtin University of Technology, Monash University, and the Australian Astronomical Observatory. SkyMapper is owned and operated by The Australian National University's Research School of Astronomy and Astrophysics. The survey data were processed and provided by the SkyMapper Team at ANU. The SkyMapper node of the All-Sky Virtual Observatory (ASVO) is hosted at the National Computational Infrastructure (NCI). Development and support the SkyMapper node of the ASVO have been funded in part by Astronomy Australia Limited (AAL) and the Australian Government through the Commonwealth's Education Investment Fund (EIF) and National Collaborative Research Infrastructure Strategy (NCRIS), particularly the National eResearch Collaboration Tools and Resources (NeCTAR), and the Australian National Data Service Projects (ANDS).

The high dispersion spectra presented herein were obtained at the W.M. Keck Observatory, which is operated as a scientific partnership among the California Institute of Technology, the University of California, and the National Aeronautics and Space Administration. The Observatory was made possible by the generous financial support of the W.M. Keck Foundation.

The authors wish to recognize and acknowledge the very significant cultural role and reverence that the summit of Mauna Kea has always had within the indigenous Hawaiian community. We are most fortunate to have the opportunity to conduct observations from this mountain.

We also acknowledge the traditional owners of the land on which the SkyMapper telescope stands, the Gamilaraay people, and pay our respects to elders past and present.

REFERENCES

Amarsi A. M., Lind K., Asplund M., Barklem P. S., Collet R., 2016, MNRAS, 463, 1518
Amarsi A. M., Nordlander T., Barklem P. S., Asplund M., Collet R., Lind K., 2018, A&A, 615, A139
Aoki W. et al., 2013, AJ, 145, 13
Asplund M., 2005, ARA&A, 43, 481
Asplund M., Grevesse N., Sauval A. J., Scott P., 2009, ARA&A, 47, 481
Barklem P. S. et al., 2005, A&A, 439, 129
Baumueller D., Gehren T., 1997, A&A, 325, 1088
Beers T. C., Preston G. W., Shectman S. A., 1992, AJ, 103, 1987
Bessell M. S. et al., 2015, ApJ, 806, L16

Bessell M., Bloxham G., Schmidt B., Keller S., Tisserand P., Francis P., 2011, PASP, 123, 789
Casey A. R., Schlaufman K. C., 2017, ApJ, 850, 179
Castelli F., Kurucz R. A., 2004, preprint (astro-ph/0405087)
Christlieb N., Schörck T., Frebel A., Beers T. C., Wisotzki L., Reimers D., 2008, A&A, 484, 721
Demarque P., Woo J.-H., Kim Y.-C., Yi S. K., 2004, ApJS, 155, 667
Dopita M. A. et al., 2010, Ap&SS, 327, 245
Frebel A., 2010, Astron. Nachr., 331, 474
Frebel A., Norris J. E., 2015, ARA&A, 53, 631
Frebel A. et al., 2006, ApJ, 652, 1585
Frebel A., Casey A. R., Jacobson H. R., Yu Q., 2013, ApJ, 769, 57
Gaia Collaboration, 2018, A&A, 616, A1
Geisler D., Smith V. V., Wallerstein G., Gonzalez G., Charbonnel C., 2005, AJ, 129, 1428
Hasselquist S. et al., 2017, ApJ, 845, 162
Howes L. M. et al., 2015, Nature, 527, 484
Howes L. M. et al., 2016, MNRAS, 460, 884
Jacobson H. R. et al., 2015, ApJ, 807, 171
Keller S. C. et al., 2007, Publ. Astron. Soc. Aust., 24, 1
Keller S. C. et al., 2014, Nature, 506, 463
Kobayashi C., Umeda H., Nomoto K., Tominaga N., Ohkubo T., 2006, ApJ, 653, 1145
Lee Y. S. et al., 2011, AJ, 141, 90
Li H., Aoki W., Zhao G. et al., 2015a, PASJ, 67, 84
Li H.-N. et al., 2015b, ApJ, 798, 110
Lind K., Asplund M., Barklem P. S., Belyaev A. K., 2011, A&A, 528, A103
Lind K., Bergemann M., Asplund M., 2012, MNRAS, 427, 50
Lind K. et al., 2017, MNRAS, 468, 4311
Marino A. F., Villanova S., Piotto G., Milone A. P., Momany Y., Bedin L. R., Medling A. M., 2008, A&A, 490, 625
McWilliam A., 1998, AJ, 115, 1640
McWilliam A., Preston G. W., Sneden C., Searle L., 1995, AJ, 109, 2757
Nordlander T., Amarsi A. M., Lind K., Asplund M., Barklem P. S., Casey A. R., Collet R., Leenaarts J., 2017, A&A, 597, A6
Norris J. E. et al., 2013, ApJ, 762, 25
Norris J. E., Yong D., Venn K. A., Gilmore G., Casagrande L., Dotter A., 2017, ApJS, 230, 28
Norris J. E., Yong D., Gilmore G., Wyse R. F. G., 2010, ApJ, 711, 350
Placco V. M., Frebel A., Beers T. C., Stancliffe R. J., 2014, ApJ, 797, 21
Roederer I. U., 2013, AJ, 145, 26
Schlaufman K. C., Casey A. R., 2014, ApJ, 797, 13
Sneden C. A., 1973, PhD thesis, Univ. Texas
Sneden C., Cowan J. J., Gallino R., 2008, ARA&A, 46, 241
Starkenburg E. et al., 2017, MNRAS, 471, 2587
VandenBerg D. A., Bergbusch P. A., Dowler P. D., 2006, ApJS, 162, 375
Vogt S. S. et al., 1994, Proc. SPIE Conf. Ser. Vol. 2198, HIRES: the high-resolution echelle spectrometer on the Keck 10-m Telescope, SPIE, Bellingham, p. 362
Wolf C. et al., 2018, PASA, 35, 10
Wolf C. et al., 2018, Publ. Astron. Soc. Aust., 35, e010
Yong D. et al., 2013, ApJ, 762, 26
Yoon J. et al., 2016, ApJ, 833, 20
Yoon J. et al., 2018, ApJ, 861, 146

SUPPORTING INFORMATION

Supplementary data are available at *MNRAS* online.

linelist_paper.tex

Please note: Oxford University Press is not responsible for the content or functionality of any supporting materials supplied by the authors. Any queries (other than missing material) should be directed to the corresponding author for the article.

This paper has been typeset from a TEX/LATEX file prepared by the author.